An Image-Based Method for Obtaining Pore-Size Distribution of Porous Media

ZHEN YANG,[†] XIAO-FENG PENG,*,[†]
DUU-JONG LEE,[‡] AND
MING-YUAN CHEN[‡]

Laboratory of Phasechange and Interfacial Transport Phenomena, Department of Thermal Engineering, Tsinghua University, Beijing 100084, China, and Chemical Engineering Department, National Taiwan University, Taipei, 106 Taiwan, China

This purpose of this investigation is to develop a new method for obtaining pore-size distribution (PSD) and other pore parameters from inner structure images. This method can be summarized into four key procedures to realize its functionality. A MATLAB program was composed to make the method applicable for image analysis. Image tests on wastewater biofouling layer samples showed the validity and feasibility of the method for analyzing intrinsic porous structures. The structural information obtained by this method can facilitate the understanding of transport phenomena, e.g., water flow and species diffusion inside porous structures.

Introduction

Structural characterization of porous media is important for a variety of practical applications, including tissue engineering, soil technology, water treatment, pharmaceutics, and so on. In these applications, both fluid flow and species transportation in porous media are closely related with inner pore configuration, such as pore shape, number and connection or networks. Most naturally formed porous materials have characteristic pore size at different scales or in a continuous distribution. For instance, pores in soil can be grouped into two types: the primary textural pore with radius of around 1 μm and the secondary structural pore of 70−80 μm (*1*). Pores having different scales are believed to contribute to distinct transport processes. Large pores favor fluid flow and contribute the most to permeability (*2*), while small pores are important for capillary, retention, matric suction, diffusion, and chemical reaction processes.

Transport phenomena (including advection and diffusion) in many environmental applications, e.g., biological wastewater treatment (*3*), sedimentation of sludge flocs (*4, 5*), as well as removal of SO_x and NO_x from flue gas (*6−8*), are greatly related with porous structures. Complex pore structures can cause distinctive flow behaviors of water flow in sludge flocs (*9−11*). To understand the influence of porous structure on transport phenomena in, but not limit to, these environmental applications, it is essential to find appropriate ways to quantitatively measure/describe the pore structure.

Pore-size distribution (PSD) is one of such critical parameters to characterize porous structures, and is often employed to describe many transport phenomena, such as water transmission and storage functions of soil (*12, 13*) and evolution of soil (*14, 15*). In the diagram of PSD, increment of pore volume is plotted against pore diameter, so the volume of pores in a small interval of diameter, Δd, near a specific diameter can be estimated. Generally, porous media with various inner structures have their own distinctive PSD maps.

The influence of PSD on transport processes arises from three aspects: pore shape, pore size and interconnection or networks. Some available investigations (*16, 17*) showed that the absorption dynamics of wetting liquids into porous media is controlled by the relative proportion of the finest pores with low aspect ratios, i.e., the ratio of pore length to diameter, and the highly connected pores. Small pores with low aspect ratios can provide capillarity acting over a short time scales in a wetting process. For example, in the computational modeling on inertial wetting terms leading to plug flow (*18*), a 0.1 μm pore with the aspect ratio of one was shown to absorb water within 10 ns (nanoseconds), while larger pores tended to induce a significant retardation due to the inertial effects. Besides pore shape and size, connection among pores also plays an important role on mass transfer in porous media. For example, in tissue engineering the minimum pore size for in vivo bone during growth into a material is thought to be 100 μm; therefore, an ideal scaffold would have interconnects of at least 100 μm in diameter between its macropores (*19−21*).

Several methods are often applied to measure PSD in the open literature, including mercury intrusion porosimeter (MIP), liquid extrusion porosimeter (LEP), size-exclusion chromatography (SEC) (*22*), nitrogen adsorption isotherms (NAI) (*23, 24*), water vapor desorption isotherms (WVDI) (*25*). MIP and LEP need exerting pressure on a test sample and therefore may change or even destroy the original structure of a sample. In addition, these two methods are only suitable to measure pore network with pore size gradually constricting from the exterior to the interior of a sample. SEC uses large molecules of different sizes as the probe, so it can only detect pores of molecular size. NAI and WVDI are used to probe pore structure below one micrometer, and their applications are restricted to specific performing conditions. For example, NAI is measured at the temperature of liquid Nitrogen (−195.82 °C) in a range of relative pressure from $p/p_o = 0.004$ to $p/p_o = 0.997$ (*1*).

In addition to their own specific constraints, all of the above methods need the test sample to be mechanically rigid and also chemically/biologically stable. These requirements cannot be met if samples are fragile and reactive, such as biotissues. Furthermore, in some applications where the complete and unaltered sample structures are of main concern, such as samples in clinical trials, it is imperative to measure the sample structure using nondestructive methods, so as to maintain the integrity of the original structure.

In the present investigation, a new method based on image analysis was developed to measure PSD of general porous structures. The method is developed to provide PSD information similar to that obtained by a mercury intrusion test, and can be applied to any kind of porous geometries. As an example of its applications, this method was employed to analyze the complex structure of a biofouling layer formed on the surface of a filtration membrane during wasterwater treatment.

* Corresponding author phone/fax: +86-10-6278-9751; e-mail: pxf-dte@mail.tsinghua.edu.cn.
  [†] Tsinghua University.
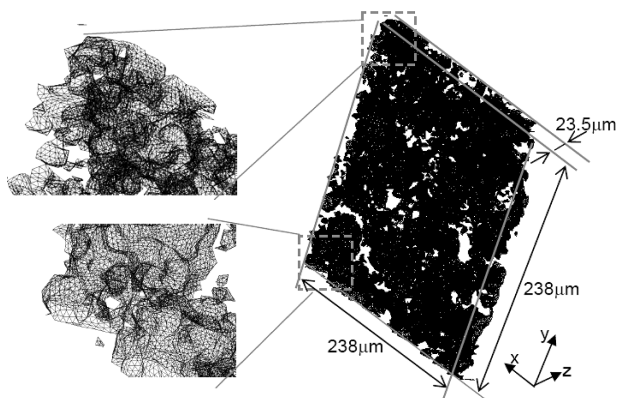 [‡] National Taiwan University.
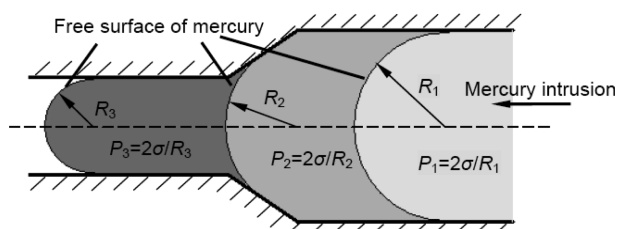
FIGURE 1. Reconstructed 3-D fouling layer.

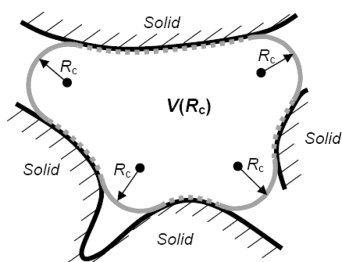**FIGURE 2. Mechanism of mercury intrusion porosimeter (MIP).**

FIGURE 3. Enclosed pore volume at a curvature radius of R_c.

Experimental Section

Experiments were designed to obtain images of the inner structure of a biofouling layer. Details on sample preparation, staining, and CLMS imaging, can be found in our previous work (*26*). So it will not be introduced in this work for the sake of brevity.

The 3-D structure of the test fouling layer was constructed from four series (β-D-glucopyranose, proteins, nucleic acids, and α-polysaccharides) of CLSM images. First, each series of CLSM images (255 grayscale format, 512 × 512 pixels in resolution, 47 images in total scanned at uniform intervals in the layer thickness direction) were converted into bileveled images using Otsu's method (*27*). In the bileveled images, white pixels (one in pixel value) represent pore area, while black pixels (zero in pixel value) are solid mass. Second, the bileveled images having the same sequential number in each series were combined into a single image. During the combination, the value of a pixel is set to zero if its value in the four serial is always zero; otherwise, the pixel value is set to one. In this way, a new composite series of bileveled images was obtained, in which pixels having a value of one are truly pore areas, i.e., none of the four ingredients colored by the four probes occupies the spatial positions of these pixels. The composite image series were used to construct the 3-D fouling layer structure, as shown in Figure 1. The construction procedure followed that of Chu (*28*).

Principle and Method

Mechanism. The idea of the method is further elucidated by the operating mechanism of MIP. By intruding mercury into pores, MIP can acquire information of pore volume fraction at different scales. Due to capillary resistance, mercury cannot flow spontaneously into pores of many porous materials without an internal pressure applied on it. By monitoring the increment of mercury intrusion against the applied pressure, the pore volume associated with a given pore size can be derived. Figure 2 delineates the intrusion process: first under a low pressure, P_1, mercury forms a free surface of large curvature, R_1, and occupies pores having diameter larger than R_1, then enters the medium pores of R_2 at a medium pressure P_2, and finally fills into small pores of R_3 when exerted on a large pressure P_3. Assuming a contact angle of 180 degrees, the pore size can be derived from

$$R = \frac{2\sigma}{P} \qquad (1)$$

where R is pore radius, σ mercury-vacuum surface tension, and P exerted pressure. Since the pressure P is gradually increased and the pores are sequentially captured from big size to small size, MIP is best suited to porous structures with converging pore size from the exterior to the interior of test samples.

Method. The 3-D structural information of the biofouling layer shown in Figure 1 is completely stored in an image series which consists of cross-sectional images at different heights in the z-direction. An image series is actually a three-dimensional orthogonally defined mathematic matrix $A(x, y, z)$ with the first and second indices x and y pointing to the pixel ID in each cross-sectional image, and the third index z to the sequential number of the image. Since the image series for the 3-D structure in Figure 1 includes 47 images of 512 × 512 pixels in resolution, the ranges of the three indices can be determined as [1, 512] for x and y, and [1, 47] for z. Note that the corresponding physical resolution of pixel is 0.465 μm/pixel in the x and y directions, and 0.500 μm/pixel in the z direction. Before any further treatments, $A(x, y, z)$ is resized to $A'(x, y, z)$ with new ranges of x, y, and z [1, 255], [1, 255], and [1, 25], respectively. The corresponding physical resolution for $A'(x, y, z)$ is 0.93 μm/pixel, equal in all the three directions. There are many other possible choices for determining the index range in order to equalize pixel size in all directions. Here $A'(x, y, z)$ is just chosen as an example, which is sufficient for testing of the proposed method for PDS analysis.

Analogous to the mechanism of MIP, a new method to measure PSD is proposed and its procedures for PDS measurement are outlined in the following four steps.

(1) Determine the critical radius $R_{c,i}$ for each unity-valued pixel (pixel in pore region). The critical radius is defined as the maximum radius of a sphere (for 3-D structures) or a circle (for 2-D structures) that has its center at the considered pixel and covers only the unity-valued pixels, i.e., entirely contained in the pore region.

(2) For each pixel having the largest $R_{c,0}$, its surrounding pixels within the distance of $R_{c,0}$ are identified and designated as the volume/area of the largest pores.

(3) For each pixel having the second largest $R_{c,1}$, its surrounding pixels within the distance of $R_{c,1}$ are identified and denoted as the volume/area of the second largest pores if they have not been designated previously or not included in the region designated by the previous radius.

(4) Repeat step 3 for pixels having the third largest $R_{c,2}$, and then for the forth largest $R_{c,3}$...until $R_{c,i}$ reaches one pixel length.

A MATLAB program, which is given in the Supporting Information, was composed to realize the function proposed in the above four steps.

Since a continuous pore structure is discretized into pixels in a format of digital image, the decrement in R_c during the
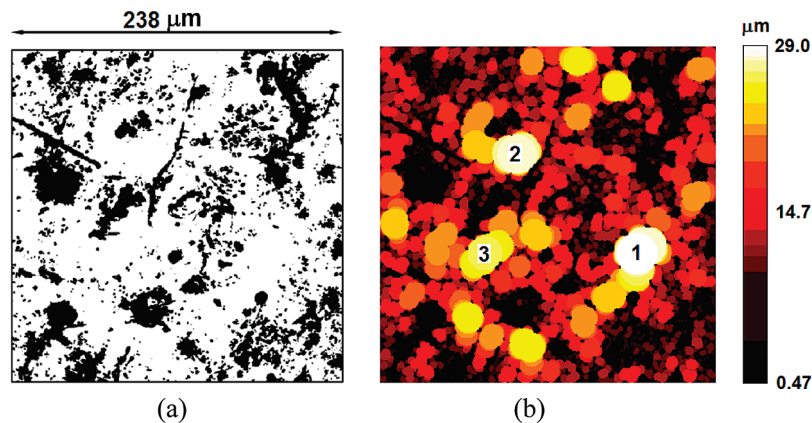
FIGURE 4. Sample 1 (cross-sectional image at 5.5 μm deep): (a) Bileveled image (pore in white), (b) color-scaled pore size (solid in black).
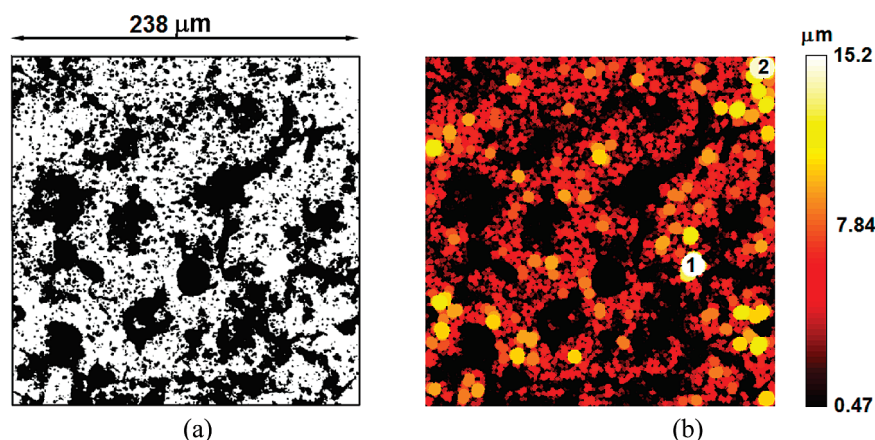

FIGURE 5. Sample 2 (cross-sectional image at 19 μm deep): (a) Bileveled image (pore in white), (b) color-scaled pore size (solid in black).
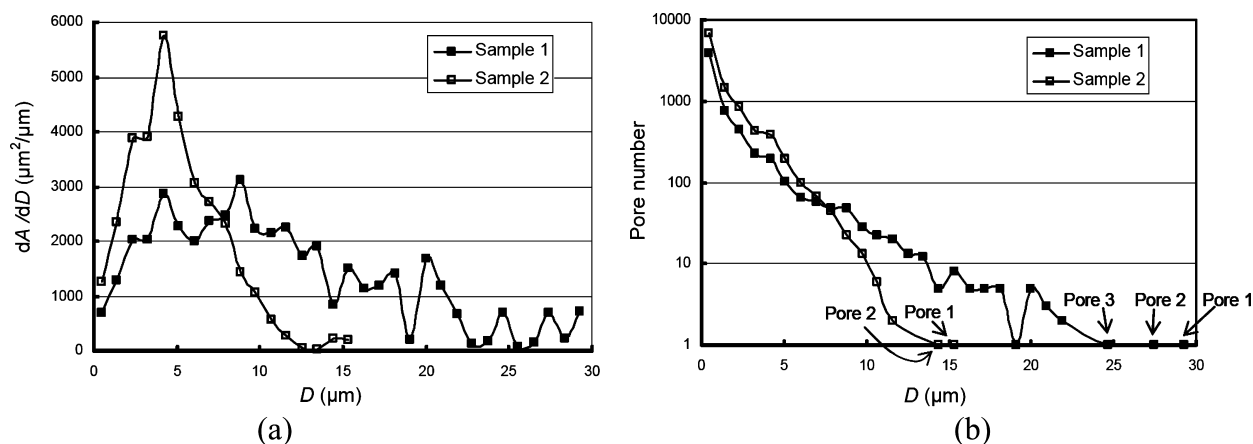

FIGURE 6. PSD analysis of the two examples (*A*, pore area, *D*, pore diameter): (a) PSD, (b) Pore number distributions.

third and fourth steps should be no smaller than one pixel size. Here the decrement in R_c is set to one pixel size. Following the above four steps, the pixel number for pores of different sizes or R_c, can be obtained. Knowing the spatial size of pixel, the volumes/areas for pores of different size can also be obtained. Furthermore, if these volumes/areas are divided by the spherical volume/circular area of the critical radius, the pore numbers at each size can be approximately estimated.

The principle of this method is explicit in a geometrical view. During the previous procedures, a serials of $R_{c,i}$ is obtained as $\{R_{c,0}, R_{c,1}, R_{c,2},..., 2, 1\}$, where $R_{c,0}$ is the maximum of R_c, and $R_{c,0} > R_{c,1} > R_{c,2},..., 2 > 1$. The decrement between any two neighboring values in the series is one pixel. Pore volume (3-D) or area (2-D) that is included in enclosed convex surfaces of curvature radius $R_{c,i}$ is a function of $R_{c,i}$, denoted here as $V(R_{c,i})$. Note the curvature radius here is not defined on the boundaries of solid mass, i.e., the gray dashed line in Figure 3, but on the boundaries in the pore region, i.e. the gray solid line in Figure 3. Also, $V(R_{c,i})$ is not necessarily one single volume and can probably be several separate volumes distributed in the porous region.

Recalling the previous four steps of the method, in the second step the pixels in $V(R_{c,0})$ are located and assigned to the largest pores of $R_{c,0}$; in the third step the pixels in the volume increment $(V(R_{c,1}) - V(R_{c,0}))$ are located and treated as volumes of pores of radius between $(R_{c,1}, R_{c,0})$; in the fourth step pixels in the volume increment of $V(R_{c,i}) - V(R_{c, i-1})$ (i
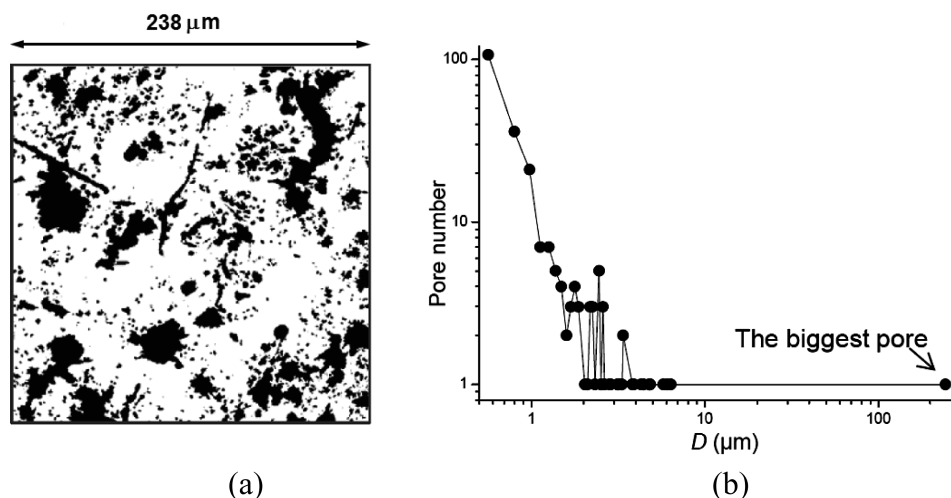
238 μm

FIGURE 7. Sample 1 investigated by the connectivity method: (a) The biggest pore (white), (b) Pore number distribution.
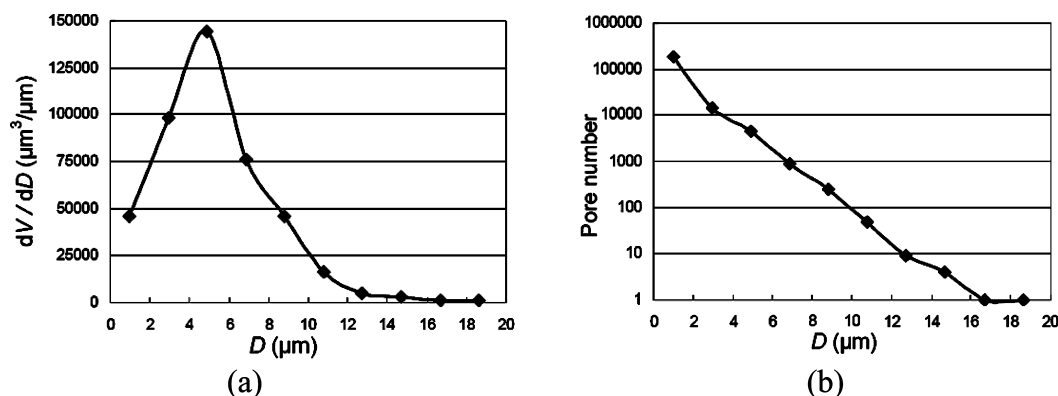

FIGURE 8. Pore characteristics of fouling layer: (a) PSD, (b) Pore number distribution. The physical size of pixels, i.e., the minimum pore size, is 0.93 μm.
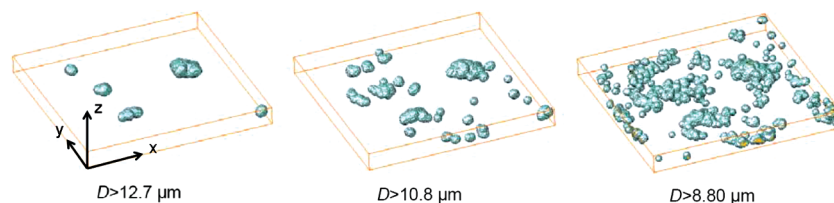

$D>12.7$ μm $D>10.8$ μm $D>8.80$ μm

FIGURE 9. Pore structures at different pore diameters.

= 2, 3,...) are sequentially located and assigned to pores of radius between $(R_{c,i}, R_{c,i-1})$. The increase of $V(R_{c,i})$ with the decrease of $R_{c,i}$ is consistent with the incursion process of mercury caused by the increasing operational pressure. Compared with the principle of MIP in Figure 2, the volume increment caused by the decrease of curvature radius or the increase of pressure is exactly the same principle that increases $V(R_{c,i})$. Similar to the definition of pore volume in MIP, the increment of $V(R_{c,i})$ is assigned as the pore volume of radius between $(R_{c,i}, R_{c,i-1})$ or diameter between (D_i, D_{i-1}) where $D_i = 2R_{c,i}$. So, pore volume per unit increment of diameter, or the derivative of pore volume with diameter, is derived as $[V(R_{c,i}) - V(R_{c,i-1})]/(D_{i-1} - D_i)$.

This method is not restricted to gradually constricting structures as required by MIP. Pixels are checked throughout the entire domain of the sample image, even for dead pores without connections to the outside, while in MIP mercury can only intrude into pores with open channels from the exterior to the interior of a test sample.

Validation. Several examples are brought up to validate the proposed method. Since the pore distributions of these examples can also be precisely obtained by mathematical analyses, they serve as the validation bases for the proposed method. The results are presented in the Supporting Information. It is found that the proposed method is precise and able to handle various geometries. Despite the error coming from using discrete pixels to resolve continuous curved surface, the proposed model should be strictly precise.

PSD Analyses on Biofouling Layers

A significant test of the proposed method is to measure the pore configuration of naturally formed complex porous structures. The biofouling layer structure prepared in the experiment part of this paper is used as a sample with an intrinsic porous structure for PSD analysis. The cross-sectional structure of the biofouling layer is obtained from the bileveled CLMS 2-D images, and the entire 3-D structure is constructed from the image series.

2-D PSD Analysis. Two typical images were selected as samples for 2-D pore structure analysis: one was at 5.5 μm deep from the top surface of the fouling layer, denoted as sample 1 (Figure 4 (a)), and the other was at 19.0 μm deep,

denoted as sample 2 (Figure 5 (a)). The pore configurations in the two images are so complex that no theoretical approach can be applied to calculate their PSDs. However, the proposed method (program) can be used to easily obtain PSD of such complex porous structures. Figures 4 (b) and 5 (b) show the pore patterns at different sizes which were obtained by applying the proposed method. Pore diameters are represented at a color scale. Evident difference in pore configuration can be observed from these two images. Large pores of diameter more than 20 μm show in sample 1 (Figure 4 (b)), while only pores of smaller than 20 μm exist in sample 2 (Figure 5 (b)). More details can be extracted by observing PSD and pore number distributions, as shown in Figures 6 (a) and (b), respectively. The PSD of sample 1 ranges from 0.47 (the physical size of pixels in 2-D images here) to 29 μm, and this range is much more extensive than that of sample 2 which only covers a range of 0.47~15.2 μm. Also, sample 1 has several peaks and a relatively even distribution of pore area, whereas sample 2 has only one peak at the pore diameter of 4.5 μm. Apparently, the numbers of large pores are not many. Sample 1 has three large pores, as indicated in Figure 4 (b) assigned as 1, 2, and 3. Similarly, sample 2 has two large pores, as numbered 1 and 2 in Figure 5 (b). These largest pores are also pointed out in the pore number distribution plots in Figure 6 (b). Both PSD and the pore number distributions show that sample 1 predominantly consists of large pores, whereas sample 2 has mostly small and medium pores. If pores smaller than 0.47 μm are of concern in PSD, images with finer resolution, e.g., 0.1 μm/pixel, are required.

As shown in the previous demonstrations, the proposed method can provide a reasonable segregation within complex porous structures with pores highly connected with each other. It can effectively solve the confusion on how to define a pore, and give an explicit definition on local pore structures, such as the three large pores in Figure 4 (b). Other methods may misinterpret pore structures when dealing with complicated geometries. For instance, one way to define a pore is based on the criterion that connected pixels comprise one single pore. In a digital image format, two pixels are connected when they have a common edge. Using this method, one largest pore can each be identified for sample 1 and sample 2. Figure 7 shows the result of the connectivity method for sample 1. The biggest pore obtained in this way covers most of the pore area, and exceed 99% the total pore area of sample 1. Defining such a biggest pore is meaningless because it acts much more like a group of small pores rather than a single pore, both from the viewpoints of geometry and flow dynamics.

3-D PSD Analysis. Figure 8 presents the PSD and pore number distribution for the 3-D biofouling layer structure in Figure 1. The pore volume of 5 μm-diameter is the largest, indicating a large portion of pore volume comes from small holes, gaps or corners. These volumes are probably adverse to fluid flows through the fouling layer. Only a few large pores of diameter over 15 μm are observed in this fouling layer. Although their volume contribution is very low, large pores may play a substantial role in fluid flows through the fouling layer. Detailed analysis of the dependence of flow behavior on pore size in the biofouling layer can be found in Yang's work (2).

Figure 9 shows the pore morphologies at different diameters. Apparently, small pore structures are well resolved when the pore diameter D decreases.

In summary, the proposed method could be conveniently applied to analyze 2-D and 3-D pore structures for intrinsic porous media, like various porous biomaterials, of which images of structures can be acquired using microscope, CLMS, micro-CT or in other photographic ways. This may provide a feasible path for further understanding of structural influence on transport processes inside these porous structures. Accuracy of the method is limited by image resolution, i.e., the minimum pore size detected by the method equals to the physical size of pixels in the image.

Supporting Information Available
Validation of the proposed method. Matlab program for the proposed method. This material is available free of charge via the Internet at http://pubs.acs.org.

Literature Cited

(1) Hajnos, M.; Lipiec, J.; Swieboda, R. Complete characterization of pore size distribution of tilled and orchard soil using water retention curve, mercury porosimetry, nitrogen adsorption, and water desorption methods. *J. Geoderma* **2006**, *135*, 307–314.

(2) Yang, Z.; Peng, X. F.; Chen, M. Y.; Lee, D. J.; Lai, J. Y. Intra-layer flow in fouling layer on membranes. *J. Membr. Sci.* **2007**, *287*, 280–286.

(3) Adav, S. S.; Lee, D. J.; Show, K. Y. Aerobic granular sludge: Recent advances. *J. Biotech. Adv.* **2008**, *26*, 411–423.

(4) Chu, C. P.; Lee, D. J. Advective flow in a sludge floc. *J. Colloid Interface Sci.* **2004**, *227*, 387–395.

(5) Chung, H. Y.; Chu, C. P.; Lee, D. J. Drag force on activated sludge floc under crossflow. *J. Chin. Inst. Chem. Eng.* **2004**, *35*, 225–230.

(6) Yan, Y.; Peng, X. F.; Lee, D. J. Transport and reaction characteristics in flue gas desulfurization. *J. Therm. Sci.* **2003**, *42*, 943–949.

(7) Sumathi, S.; Bhatia, S.; Lee, K. T. Performance of an activated carbon made from waste palm shell in simultaneous adsorption of SOx and NOx of flue gas at low temperature. *Sci. China Ser. E* **2009**, *52*, 198–203.

(8) Kiel, J. H. A.; Prins, W.; Vanswaaij, W. P. M. Performance of silica-supported copper-oxide sorbents for SO$_x$/NO$_x$-removal from flue-gas 0.1. sulfur-dioxide absorption and regeneration kinetics. *App. Catal., B* **1992**, *1*, 13–39.

(9) Yang, Z.; Peng, X. F.; Lee, D. J.; Su, A. Advective flow in spherical floc. *J. Colloid Interface Sci.* **2007**, *308*, 451–459.

(10) Yang, Z.; Peng, X. F.; Lee, D. J.; Su, A. Reynolds number-dependent permeability of wastewater sludge flocs. *J. Chin. Inst. Chem. Eng.* **2007**, *38*, 135–141.

(11) Yang, Z.; Peng, X. F.; Chu, C. P.; Lee, D. J.; Su, A. Sedimentation of permeable floc. *Drying Technol.* **2006**, *24*, 1277–1282.

(12) Mallants, D.; Tseng, P. H.; Toride, N.; Timmerman, A.; Feyen, J. Evaluation of multimodal hydraulic functions in characterizing a heterogeneous field soil. *J. Hydrol.* **1997**, *195*, 172–199.

(13) Droogers, P.; Stein, A.; Bouma, J.; Boer, G. Parameters for describing soil macroporosity derived from staining patterns. *J. Geoderrma* **1998**, *83*, 293–308.

(14) Velde, B.; Moreau, E.; Teribile, F. Pore networks in an Italian vertisol: quantitative characterisation by two dimensional image analysis. *J. Geoderma* **1996**, *72*, 271–285.

(15) Richard, G.; Cousin, I.; Sillon, J. F.; Bruand, A.; Guerif, J. Effect of compaction on soil porosity: consequences on hydraulic properties. *Eur. J. Soil Sci.* **2001**, *52*, 49–58.

(16) Ridgway, C. J.; Gane, P. A. C.; Schoelkopf, J. Effect of capillary element aspect ratio on the dynamic imbibition with porous networks. *J. Colloid Interface Sci.* **2002**, *252*, 373–382.

(17) Schoelkopf, J.; Ridgway, C. J.; Gane, P. A. C.; Matthews, G. P.; Spielmann, D. C. Measurement and network modeling of liquid permeation into compacted mineral blocks. *J. Colloid Interface Sci.* **2000**, *227*, 119–131.

(18) Schoelkopf, J.; Gane, P. A. C.; Ridgway, C. J.; Matthews, G. P. Influence of inertia on liquid absorption into paper coating structures. *Nord. Pulp Pap. Res. J.* **2000**, *15*, 422–430.

(19) Hulbert, S. F.; Morrison, S. J.; Klawitte, J. J. Tissue Reaction to 3 ceramics of porous and non-porous structures. *J. Biomed. Mater. Res.* **1972**, *6*, 347–374.

(20) Freyman, T. M.; Yannas, I. V.; Gibson, L. J. Cellular materials as porous scaffolds for tissue engineering. *Prog. Mater. Sci.* **2001**, *46*, 273–282.

(21) Holy, C. E.; Shoichet, M. S.; Davies, J. E. Engineering three-dimensional bone tissue in vitro using biodegradable scaffolds: investigating initial cell-seeding density and culture period. *J. Biomed. Mater. Res.* **2000**, *51*, 376–382.

(22) Yao, Y.; Lenhoff, A. M. Determination of pore size distributions of porous chromatographic adsorbents by inverse size-exclusion chromatography. *J. Chromatogr., A* **2004**, *1037*, 273–282.

(23) Greeg, S. J.; Sing, K. S. W. *Adsorption, Surface Area and Porosity*; Acad. Press: New York, 1982.

(24) Ościk, J. *Adsorption*; Ellis Horwood: Chichester, 1982.

(25) Naono, H.; Hakuman, M. Analysis of porous texture by means of water vapor adsorption isotherm with particular attention to lower limit of hysteresis loop. *J. Colloid Interface Sci.* **1993**, *158*, 19–26.

(26) Chen, M. Y.; Lee, D. J.; Yang, Z.; Peng, X. F.; Lai, J. Y. Fluorecent staining for study of extracellular polymeric substances in membrane biofouling layers. *Environ. Sci. Technol.* **2006**, *40*, 6642–6646.

(27) Otsu, N. A threshold selection method from gray-level histogram. *IEEE Trans. Syst. Man. Cybern.* **1979**, *9*, 62–66.

(28) Chu, C. P.; Lee, D. J.; Tay, J. H. Floc model and intrafloc flow. *Chem. Eng. Sci.* **2005**, *60*, 565–575.